Plasmonic Effects of Metallic Nanoparticles on Enhancing Performance of Perovskite Solar Cells

Qi Luo,[†] Chenxi Zhang,[†] Xueshuang Deng,[†] Hongbing Zhu,[‡] Zhiqiang Li,[‡] Zengbo Wang,[§] Xiaohong Chen,[†] and Sumei Huang*,[†]

[†]Engineering Research Center for Nanophotonics & Advanced Instrument, Ministry of Education, School of Physics and Materials Science, East China Normal University, North Zhongshan Rd. 3663, Shanghai 200062, P. R. China
[‡]Institute of Photovoltaics, College of Physics Science and Technology, Hebei University, Baoding 071002, P. R. China
[§]School of Electronic Engineering, Bangor University, Bangor LL57 1UT, U.K.

ABSTRACT: We report systematic design and formation of plasmonic perovskite solar cells (PSCs) by integrating Au@TiO$_2$ core−shell nanoparticles (NPs) into porous TiO$_2$ and/or perovskite semiconductor capping layers. The plasmonic effects in the formed PSCs are examined. The most efficient configuration is obtained by incorporating Au@TiO$_2$ NPs into both the porous TiO$_2$ and the perovskite capping layers, which increases the power conversion efficiency (PCE) from 12.59% to 18.24%, demonstrating over 44% enhancement, compared with the reference device without the metal NPs. The PCE enhancement is mainly attributed to short-circuit current improvement. The plasmonic enhancement effects of Au@TiO$_2$ core−shell nanosphere photovoltaic composites are explored based on the combination of UV−vis absorption spectroscopy, external quantum efficiency (EQE), photocurrent properties, and photoluminescence (PL). The addition of Au@TiO$_2$ nanospheres increased the rate of exciton generation and the probability of exciton dissociation, enhancing charge separation/transfer, reducing the recombination rate, and facilitating carrier transport in the device. This study contributes to understanding of plasmonic effects in perovskite solar cells and also provides a promising approach for simultaneous photon energy and electron management.

KEYWORDS: perovskite solar cells, Au nanoparticles, exciton generation, exciton dissociation, plasmon enhancement, near-field
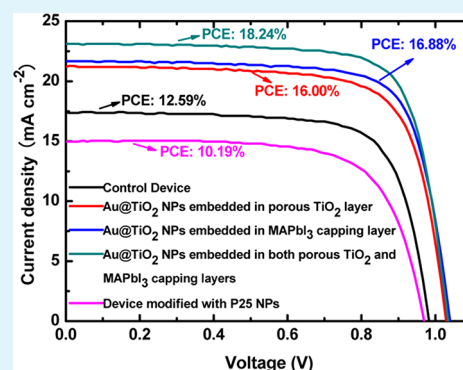
1. INTRODUCTION

Solar energy technologies have the potential to meet a large portion of future energy needs and make a contribution to solving the global energy crisis and environmental problems. Recently, perovskite solar cells (PSCs) have received significant research interest owing to their high solar conversion efficiencies and low-cost fabrication methods. Starting from the first well-known PSCs which employed the device structure of dye-sensitized solar cells (DSSCs) by using perovskite nanocrystals to replace traditional organic dye molecules as sensitizers in 2009, in only seven years power conversion efficiencies (PCEs) above 22% have already been reported and certified.[1−4] Such rapid and unprecedented progress in solar conversion efficiencies was achieved through the fabrication of a dense, uniform, and high quality perovskite absorber layer with a variety of fabrication techniques, including spin coating,[2] dip coating,[5] two-step interdiffusion,[6] chemical vapor deposition,[7] thermal evaporation,[8] solvent engineering,[9,10] and intramolecular exchange processing.[11] Specially, a high-quality perovskite capping layer was introduced to optimize the morphology of the absorber material and improve the device performance.[5,10] Even though perovskite absorbers can efficiently apply visible light in perfectly designed and fabricated

devices, further improvements for PSCs are expected and required in order to completely surpass the other photovoltaic (PV) technologies, such as silicon, GaAs, CIGS, and CdTe solar cells, and fully realize their potential as PV cells.

The utilization of metallic nanostructures in solar cells provides opportunities to revolutionize the conversion of solar energy by enabling highly efficient devices either via scattering light to enable a longer optical path length or via a dipole−dipole interaction and resonant energy transfer.[12] Metallic nanostructures have been successfully employed to moderately improve the performance of dye-sensitized solar cells,[13,14] silicon-based solar cells,[15,16] and organic[17] photovoltaic (OPV) cells. It is well-known that the size, shape, component, and dielectric environment of metal nanostructures play very important roles in affecting photovoltaic performance. In terms of plasmonic organic photovoltaic devices, since the earliest reports,[18,19] plasmonics have been applied in various configurations within organic solar cells, exhibiting benefits which extend beyond light absorption enhancements, to

improved electrical characteristics, such as increased conductivity of buffer layers and enhanced exciton dissociation.[20−25] Recently, metallic nanostructures have also been employed to improve the PCE of PSCs. Snaith and co-workers first reported plasmonic enhancement in perovskite solar cells in 2013.[26] They mixed core−shell Au@SiO$_2$ nanoparticles (NPs) into Al$_2$O$_3$ paste to prepare mesoporous Al$_2$O$_3$ scaffold and fabricated meso-superstructured PSCs, of which the average PCE was enhanced from 8.5% to 9.5%. The enhancement in device performance was attributed to a reduction in exciton binding energy (EB) of the perovskite in the presence of nano-Ag localized surface plasmon resonance (LSPR). Later, the group blended Ag@TiO$_2$ NPs into Al$_2$O$_3$ paste to prepare mesoporous Al$_2$O$_3$ scaffold, boosting the CH$_3$NH$_3$PbI$_{3−x}$Cl$_x$ device efficiencies by 12.4%.[27] But their analysis suggested PV performance enhancement is different. In another study,[28] Au NPs were inserted into a compact titanium dioxide layer, resulting in 20% device performance enhancement in planar heterojunction CH$_3$NH$_3$PbI$_{3−x}$Cl$_x$ solar cell. The device performance enhancement was attributed to plasmon-mediated hot carrier injection from Au NPs to titanium dioxide. Cheng et al. also embedded metallic nanostructures (nanostructured Au, Ag, and Au−Ag) into a compact TiO$_2$ layer, achieving an efficiency of 14.8% using the Au−Ag nanoalloy, which increases 17.5% compared to the bare PSCs.[29] The increased device performance was attributed to the increased light harvesting due to the light scattering of the metallic nanostructures. Nevertheless, their analysis is different from that reported in ref 28. Lee et al. reported just 0.6% PCE improvement by introducing Au NPs into the hole-transport layer of PSCs, from 12.66% to 12.74%.[30] Recently, we reported a facile and effective method to fabricate efficient plasmonic PSC devices.[31] The combinational integration of Au NPs and MgO into mesoporous titania significantly enhanced both the current density and the photovoltage of the perovskite solar cells.[31] Current reports on plasmonic applications in PSCs focused on integration of metal (Au, Ag) nanoparticles within the mesoporous metal oxide scaffolds or the charge transport layers to improve device performance. These initial studies indicate that the presence of metal particles somehow favors a reduction in exciton binding energy,[26] photon recycling,[27,31] hot carrier injection from metal NPs,[28] and increasing the light harvesting capability;[29] however, the origin of the PV performance enhancement observed remains unclear. Additionally, metal inclusions in absorbers can induce intrinsic losses of metals at visible frequencies and recombination centers, leading to unexpected efficiency losses.[32] The question remains as to whether plasmonic NPs are able to overcome their negative effects to achieve effective efficiency enhancements, especially when embedded into pure perovskite semiconductors. Integration of plasmonic nanostructures into perovskite solar cells is a relatively new concept, compared to the body of published work on organic solar cells, and many fundamental physical mechanisms are not systematically understood.

In this work, we developed a new and efficient plasmonic composite structure to effectively enhance the PCE of PSCs by synchronously incorporating core−shell metal−dielectric nanoparticles into both the porous TiO$_2$ film and the perovskite capping layer. Au@TiO$_2$ core−shell nanoparticles were synthesized and integrated into porous TiO$_2$ and/or perovskite semiconductor capping layers to form plasmonic PSC devices with different configurations. Optical, electrical, and electronic effects from metal nanostructures on the device performance of PSCs were systematically investigated by a combined evaluation of surface morphologies of Au@TiO$_2$ modified porous TiO$_2$ and perovskite capping films, photovoltaic characteristics, photocurrent behavior, and steady-state photoluminescence (PL). The addition of Au@TiO$_2$ NPs increased the rate of exciton generation and the probability of exciton dissociation, thereby enhancing the short-circuit current density and the fill factor. Accordingly, when 80 nm sized Au@TiO$_2$ NPs were simultaneously incorporated into both mesoporous titania and perovskite capping layers in the devices, the power conversion efficiency (PCE) was improved from 12.59% to 18.24%, demonstrating over 44% enhancement, compared with the reference device without the metal NPs. The results offer a possible method to dramatically enhance the performance of mesoporous PSC devices by employing metal nanoparticles and provide further insight into the development of ideal plasmonic functionality for future optoelectronic systems.

2. EXPERIMENTAL SECTION

2.1. Synthesis of Core@ShellAu@TiO$_2$ NPs. Au nanoparticles were prepared according to the method published previously with slight modification.[31] A 972 μL portion of hydrogen tetrachloroaurate-(III) (HAuCl$_4$·4H$_2$O) aqueous solution (0.1 M) was mixed with deionized (DI) water (80 mL) and ethylene glycol (200 mL) in a flask, and then 4 mL of 1 wt % trisodium citrate dehydrate solution and 4 mL of 1 wt % polyvinylpyrrolidone K30 (PVP-K30) were added. After this, the mixture was brought to a rolling boil with stirring for about 10 min; the reduction of gold chloride was almost completed. The solution was removed from the heat source and allowed to cool naturally. The obtained mixture was collected by centrifugation at 8000 rpm, followed by washing with ethanol and DI water for three times. The precipitate was redispersed in 48 mL of isopropanol as a stock solution of Au core. The diameter of the obtained Au nanoparticles is about 80 nm.

TiO$_2$ shell layer was further coated on the surface of Au core by a kinetics-controlled hydrolysis of titanium isopropylate (TTIP) using ammonium hydroxide as a hydrolysis catalyst.[33] The thickness of the TiO$_2$ shell can be readily varied by controlling the reaction time as well as the added amounts of hydrolysis catalyst and Ti precursor.[34] In our work, the shell thickness was controlled at about 2 nm through adjusting the amount of TTIP. NH$_3$·3H$_2$O solution (18 mL, 10 wt %) was mixed with the stock solution of Au core (48 mL) in a flask. After stirring for about 30 min, 16 mL of isopropanol solution containing 20 μL of TTIP was added dropwise into the above suspension liquid within 20 min and further stirred for 24 h. Then, the resultant product was divided equally into two parts and collected by centrifugation at 8000, followed by washing with ethanol and DI water for three times. After this, the two parts of the product were redispersed in 1.6 mL of anhydrous ethanol (30 mmol L$^{−1}$ of Au@TiO$_2$ NPs) and 1.6 mL of γ-butyrolactone (GBL)/dimethyl sulfoxide (DMSO) (7:3 v/v) solution (30 mmol L$^{−1}$ of Au@TiO$_2$ NPs). The thickness of TiO$_2$ shell is about 2 nm for Au@TiO$_2$ NPs.

2.2. Device Fabrication. Fluorine-doped tin oxide (FTO)-coated slides (Pilkington TEC 15) were patterned by etching with Zn powders and 2 M HCl. The etched slides were then cleaned with liquid detergent, acetone, ethyl alcohol, and DI water for 15 min, sequentially, to remove the organic or inorganic residues and finally dried in a vacuum oven. TTIP (200 μL) and ethanol (5 mL) were mixed to prepare a clear precursor sol. The precursor sol was spin-coated onto the etched FTO substrate at 4500 rpm, followed by annealing at 500 °C to form a compact TiO$_2$ (c-TiO$_2$) layer. Diluted TiO$_2$ pastes were prepared by mixing TiO$_2$ paste (Dyesol 18NR-T, 0.1 g) and anhydrous ethanol (444 μL). Diluted TiO$_2$ pastes with Au@TiO$_2$ NP modification were prepared by mixing TiO$_2$ paste (Dyesol 18NR-T, 0.1 g) and the prepared ethanol solution of Au@TiO$_2$ (444 μL). The mesoporousTiO$_2$ (p-TiO$_2$) layer was deposited on the c-

Scheme 1. Schematic of Five Types of PSC Devices
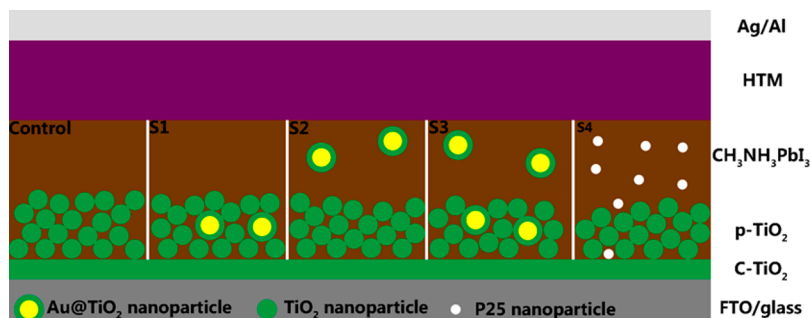
TiO$_2$ layer by spin-coating the diluted TiO$_2$ pastes without or with the addition of Au@TiO$_2$ NPs at 2000 rpm for 30 s. The layers were then sintered at 500 °C for 30 min in air. After cooling down to the room temperature (RT), the samples were treated using the TiCl$_4$ aqueous solution at 70 °C for 30 min and dried at 500 °C for 30 min. As a result, two types of p-TiO$_2$ electrodes were grown, including the bare p-TiO$_2$ and the p-TiO$_2$ containing Au@TiO$_2$ NPs. The perovskite MAPbI$_3$ absorber was grown via a spin-coating process using a GBL/DMSO solution of PbI$_2$ and CH$_3$NH$_3$I. A pure perovskite–precursor solution (1.25 mol L^{-1}) was prepared by mixing MAI (0.1975 g) powders and lead iodide PbI$_2$ (0.5785 g) in GBL (700 µL) and DMSO (300 µL) at 60 °C for 12 h. In addition, Au@TiO$_2$ and P25 TiO$_2$ NP modified perovskite–precursor solutions were prepared. To prepare the Au@TiO$_2$ NP modified perovskite–precursor solution, the MAI (0.1975 g) powders and lead iodide PbI$_2$ (0.5785 g) in GBL (350 µL) and DMSO (150 µL) were mixed with the prepared GBL/DMSO solution of Au@TiO$_2$ (500 µL) at 60 °C for 12 h. To prepare the P25 NP modified perovskite–precursor solution, the MAI (0.1975 g) powders and lead iodide PbI$_2$ (0.5785 g) in GBL (350 µL) and DMSO (150 µL) were mixed with 500 µL of a P25 GBL/DMSO (7:3 v/v ratio) solution (30 mmol L^{-1}) at 60 °C for 12 h. The formed precursor solution was deposited onto the p-TiO$_2$/c-TiO$_2$/FTO sample via a successive two-step spin-coating process, at 2000 rpm for 30 s and at 3500 rpm for 50 s, respectively. Anhydrous chlorobenzene was dripped onto the center of the sample in the second spin-stage during the spin-coating process.[10] The perovskite–precursor coated sample was heated and dried on a hot plate at 110 °C for 30 min. The hole-transport material (HTM) was deposited on the grown perovskite absorber by spin-coating a spiro-OMeTAD solution at 4000 rpm for 30 s.[31] Finally, 100 nm thick Ag film with an active area of 0.1 cm^2 was formed via evaporation on the spiro-OMeTAD-coated film.[35] As a result, plasmonic PSC devices with different configurations were designed and fabricated by integrating Au@TiO$_2$ core–shell nanoparticles into the various positions of the perovskite absorber, as shown in Scheme 1.

2.3. Characterization. The morphologies of Au@TiO$_2$ NP modified p-TiO$_2$ and perovskite capping films were characterized by a high-resolution field emission scanning electron microscope (FESEM, Hitachi S4800) equipped with an energy dispersive X-ray (EDX) spectrometer. Element analysis of the composite layer was measured by the EDX. Optical spectra of p-TiO$_2$-based perovskite absorbers with various structures were examined and characterized by means of ultraviolet–visible light (UV–vis) spectrometer (Hitachi, U-3010). PL spectra were recorded at room temperature using a HORIBA JobinYvon fluoromax-4 fluorescence spectrophotometer with an excitation wavelength of 507 nm. Photocurrent density–voltage (J–V) measurements were performed using an AM 1.5 solar simulator equipped with a 1000 W xenon lamp (Model No. 91192, Oriel, USA). The solar simulator was calibrated by using a standard silicon cell (Newport, USA). The light intensity was 100 mW cm^{-2} on the surface of the test cell. J–V curves were measured using a computer-controlled digital source meter (Keithley 2440) with the reverse direction. During device photovoltaic performance characterization, a metal aperture mask with an opening of about 0.09 cm^2 was used. The external quantum efficiency (EQE) measurements (74125, Oriel, USA) were also carried out for these cells.

3. RESULTS AND DISCUSSION

FESEM was used to study the surface and the cross-sectional microstructure and morphology of the grown p-TiO$_2$, perovskite capping films, and PSC devices. Figures 1a and 1b show typical FESEM images of the top surface morphology of the formed p-TiO$_2$ layers without and with Au@TiO$_2$ NPs, and the corresponding cross-sectional FESEM pictures are displayed in Figures 1c and 1d, respectively. From Figure 1b, the size of Au@TiO$_2$ NPs (white spheres) is about 80 nm in diameter. Au@TiO$_2$ core–shell nanoparticles were integrated into the porous TiO$_2$; thus, Au@TiO$_2$ NPs were distributed both on the top surface of the p-TiO$_2$ and within the p-TiO$_2$, as shown in Figures 1b,d,e and the EDX measurements in Figures 1f,g. Thick film samples were specially grown by twice spin-coating of the prepared TiO$_2$ pastes with and without Au@TiO$_2$ NPs for convenient cross-sectional microstructure and element examination and analysis. For the Au@TiO$_2$ core–shell NPs blended within the p-TiO$_2$ layer, Au signals were clearly detected from points 1 and 2 of Figure 1e and exhibited in Figures 1f and 1g, respectively. Figures 1h and 1i show typical FESEM images of the top surface morphology of the perovskite absorber formed on the p-TiO$_2$ using perovskite precursors without and with Au@TiO$_2$ NPs. Both perovskite absorbers display a quite similar top surface morphology. The cross-sectional FESEM picture of PSCs is displayed in Figure 1j. From Figure 1j, the thicknesses of the p-TiO$_2$ and perovskite capping layers are 210 and 250 nm, respectively, almost having the same thickness. From Figure 1a, the size of the mesoporous pores of the pristine p-TiO$_2$ is about tens of nanometers, and most of the pores are smaller than 50 nm in size. These mesoporous pores can give an adequate space for the infiltration of the pure perovskite precursor and deposition of the perovskite absorber but have a limited space for the infiltration of the Au@TiO$_2$ NPs blended into the perovskite precursor. Considering the large size of the Au@TiO$_2$ core–shell NPs and the small pore size of p-TiO$_2$ layer, Au@TiO$_2$ NPs were mainly distributed in the perovskite capping layer of the absorber grown using the Au@TiO$_2$ NP modified perovskite precursor solution. Therefore, in this work, five types of perovskite solar cells were fabricated using the pristine perovskite absorber (control device): Au@TiO$_2$ NPs blended within the p-TiO$_2$ layer (S1), Au@TiO$_2$ NPs blended within the capping perovskite layer (S2), Au@TiO$_2$ NPs synchronously integrated within both the p-TiO$_2$ and the capping perovskite films (S3), and P25 NP modified the perovskite absorber (S4), as shown in Scheme 1. The absorbance of the
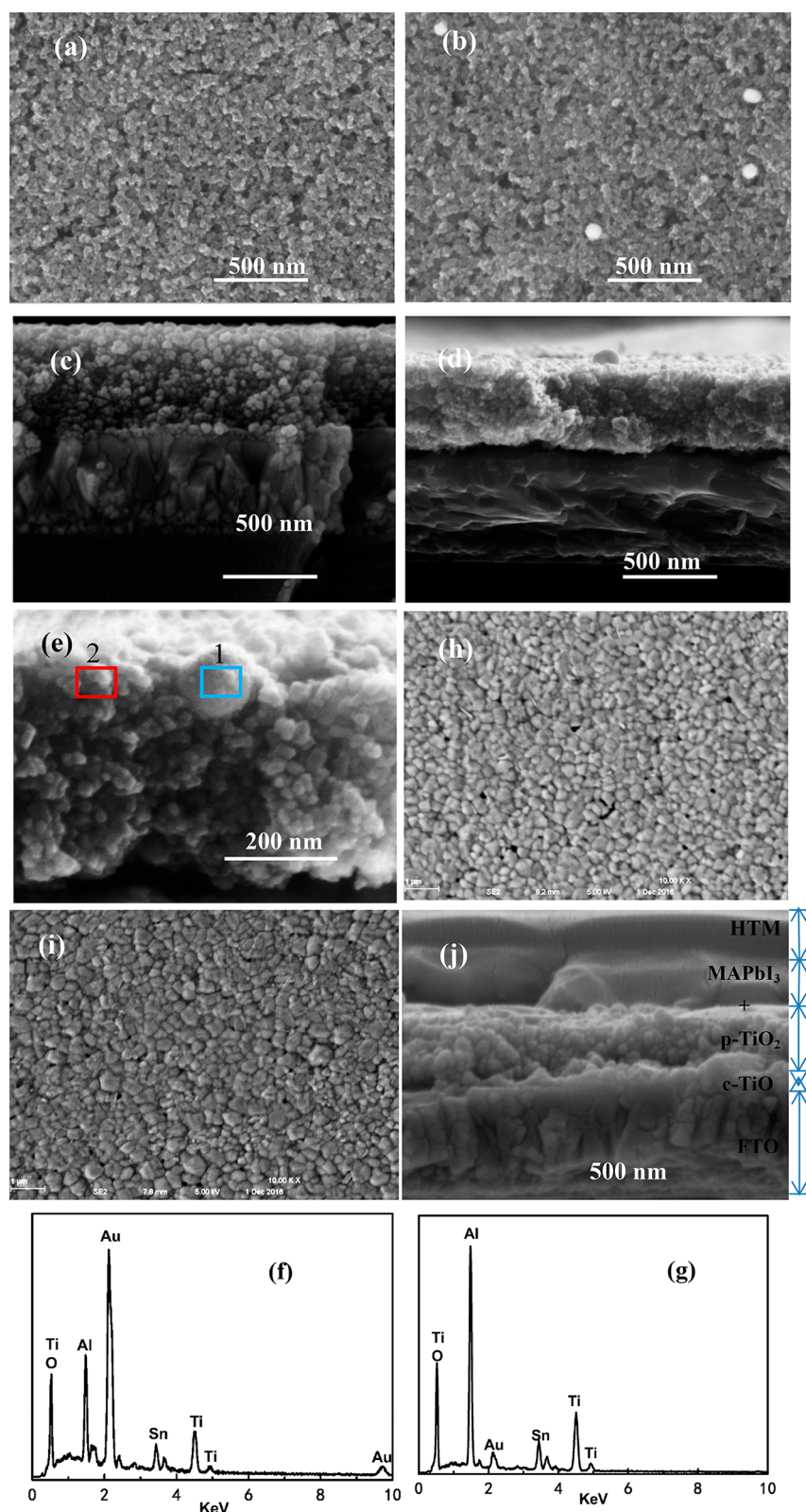
Figure 1. FESEM image of the top surface morphology of the p-TiO$_2$ layer without (a) and with (b)Au@TiO$_2$ NP modification. Cross-sectional FESEM picture of the p-TiO$_2$ without (c) and with (d, e) Au@TiO$_2$ NP modification. (f, g) EDX patterns of the p-TiO$_2$ containing Au@TiO$_2$ NPs. FESEM image of the top surface morphology of the perovskite absorber without (h) and with (i) Au@TiO$_2$ NP modification. (j) Cross-section FESEM image of the PSCs.

prepared Au and Au@TiO$_2$ NPs in ethanol is shown in Figure 2. From the figure, the SPR absorbance peak was at about 550 nm. The used concentrations of Au and Au@TiO$_2$ NPs were

equal in ethanol. The weaker SPR response of the latter was attributed to the effect of the TiO$_2$ shell of the core−shell Au@ TiO$_2$ NPs as reported in ref 36.
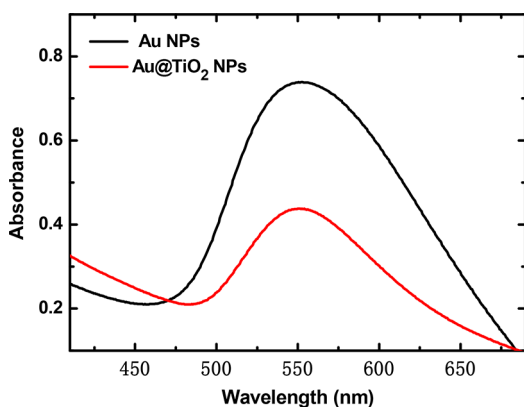
Figure 2. UV–vis absorption spectra of Au or Au@TiO$_2$ NP ethanol solutions.

Table 1. Parameters of the Best-Performing PSC Devices with Different Configurations (Control Device, S1−S4)

device	V_{OC} (V)	J_{SC} (mA cm^{-2})	FF (%)	PCE (%)	R_s(Ω)
control device	0.98	17.40	73.7	12.59	38
S1	1.03	21.20	73.3	16.00	32
S2	1.04	21.68	75.0	16.88	32
S3	1.04	23.12	75.5	18.24	30
S4	0.97	14.97	70.3	10.19	51

Figure 3a shows the current density−voltage (J−V) curves of the best-performing PSC devices with different configurations (control device, S1−S4). The corresponding PV parameters including short-circuit current density (J_{SC}), open circuit voltage (V_{OC}), PCE, and fill factor (FF) are summarized in Table 1. For each fabrication condition, 12−16 perovskite solar cells were fabricated in an identical manner. The statistics of the PCE based on more than 48 devices from four batches are shown in Figures 3b−e.

From Table 1, the control device without Au@TiO$_2$ or P25 NP modification exhibits a V_{OC} of 0.98 V, J_{SC} of 17.40 mA cm^{-2}, and FF of 73.7%, resulting in a total PCE of 12.59%. With incorporating P25 NPs into the perovskite precursor solution, the resulted PSC device (S4) became a little poorer and exhibited a PCE of 10.19%. The addition of P25 NPs obviously decreased the J_{SC}. In contrast, using Au@TiO$_2$ core−shell NPs blended within the porous TiO$_2$ layer, device S1 displayed an obviously higher average PCE of 16.00%, while using Au@TiO$_2$ NPs integrated within the capping perovskite layer, device S2 reached an even higher PCE of 16.88%. Moreover, by synchronously incorporating Au@TiO$_2$ into both the p-TiO$_2$ and the perovskite capping layers, the PV performance was further improved. From Table 1, when

Au@TiO$_2$ core−shell NPs simultaneously blended in both the p-TiO$_2$ and the perovskite capping layers, device S3 achieved a PCE of 18.24%. Compared with case of the control device, the J_{SC} value of S3 significantly increased from 17.40 to 23.12 mA cm^{-2}, the FF value improved from 73.7% to 75.5%, and the V_{OC} value increased from 0.98 to 1.04 V. The optimal cell was obtained with Au@TiO$_2$ NPs blended within both the p-TiO$_2$ and the capping perovskite layers, simultaneously. Compared with the control device, the power conversion efficiency (PCE) enhancement for the device incorporating Au@TiO$_2$ core−shell NPs into both the p-TiO$_2$ and the capping perovskite layers comes from the greatly improved short-circuit photocurrent J_{SC}. As shown in Figures 3b−e, compared with the control device, Au@TiO$_2$ NP modified devices S1, S2, and S3 exhibited higher and higher average device photovoltaic parameters such as average J_{SC}, V_{OC}, FF, and PCE. The average PCEs of device S3 and the control device are 16.90 ± 1.26% and 11.43 ± 1.14%, respectively. The average PCE of the PSCs with Au@TiO$_2$ NPs blended within both the p-TiO$_2$ and the capping perovskite layers is improved by 48% compared to that of the control PSCs.

The average primary particle size of P25 TiO$_2$ NPs is about 21 nm, which is much larger than the dimension of the colloidal TiO$_2$ NPs (about 10 nm) in the TiO$_2$ paste used for formation of the porous p-TiO$_2$ films. P25 NPs blended within the perovskite absorber may act like light scatters and have the potential to increase the light absorption; nevertheless, the addition of P25 NPs into the absorber distinctly degraded the PV performance of the PSC device, especially the short-circuit photocurrent value. The lowest J_{SC} and FF of S4 can be
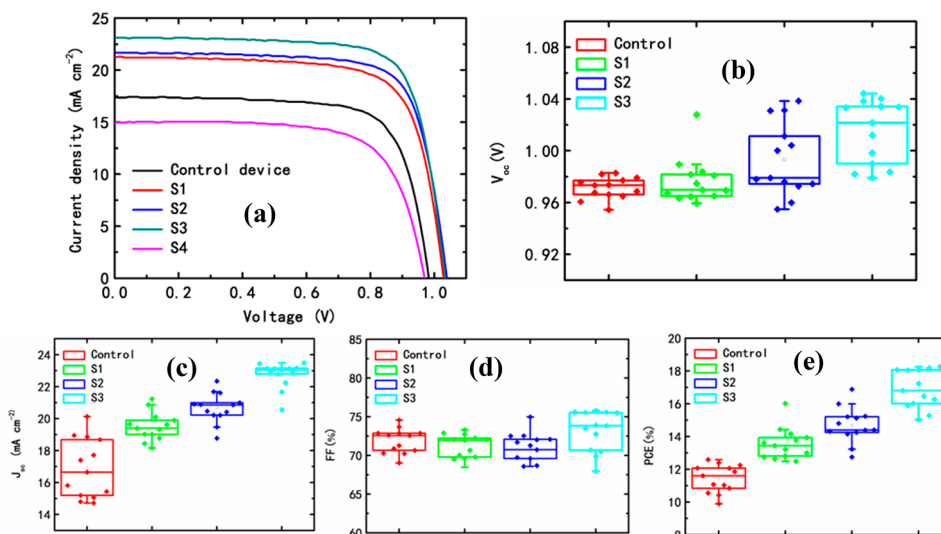

Figure 3. (a) J−V curves of the best-performing perovskite solar cells with different configurations (control device, S1−S4). Statistics of device performance parameters (b) VOC, (c) JSC, (d) FF, and (e) PCE of PSC devices with different configurations.

attributed to its highest serial resistance shown in Table 1. However, incorporating Au@TiO$_2$ core–shell NPs into either the p-TiO$_2$ or the perovskite capping layers significantly improved the PV performance. Compared with the control device, Au@TiO$_2$ NP modified devices S1, S2, and S3 exhibited considerably higher photocurrent, and device S3 shows a higher J_{SC} value than devices S1 and S2 due to the higher amount of Au@TiO$_2$ nanomaterials assembled into device S3. The photocurrent enhancement in these solar cells suggested that localized surface plasmon resonance (LSPR) and electrical effects of Au NPs enhance the photovoltaic response of PSCs.[37,38] In addition, compared to the control device, the open-circuit voltage of the device with Au@TiO$_2$ NP modification increased by 50–60 mV. This V_{OC} increase could also be associated with the plasmonic coupling between Au NPs, which may promote electron transfer to the conduction band (CB) of TiO$_2$ and change the surface potential of the latter, thus increasing the built-in potential of the device.[28] The highest FF of S3 can be associated with its lowest serial resistance shown in Table 1.

To investigate the optical and electrical effects of Au@TiO$_2$ NPs in PSC in detail, we measured optical absorption spectra as well as photoluminescence spectra of the TiO$_2$ electrodes and absorber samples. Figure 4a shows the UV–vis spectra of FTO/c-TiO$_2$/p-TiO$_2$ samples without or with Au@TiO$_2$ NP modification. Both samples display a similar light absorption, indicating that the addition of Au@TiO$_2$ NPs into the porous TiO$_2$ film had no obviously negative effect on the transparency of the p-TiO$_2$. As the PSC devices have different structures which would impact the interface between the perovskite absorber and the porous TiO$_2$, it is expected to show different defect densities. The PL spectra were effective in exploring the recombination properties of light-excited electrons and holes in defected semiconductors. Figures 4b and 4c show the UV–vis and the PL spectra of FTO/c-TiO$_2$/p-TiO$_2$/CH$_3$NH$_3$PbI$_3$ absorber samples without or with Au@TiO$_2$ NP modification. Perovskite absorbers 1–3 are with Au@TiO$_2$ NPs being blended within the p-TiO$_2$ layer, the perovskite capping layer, and both the p-TiO$_2$ and the capping perovskite films, respectively. At a glance, it is clear that there is no significant change in the absorption spectra of the four kinds of absorber samples, even in the range of specific absorption wavelengths associated with Au@TiO$_2$ NPs shown in Figure 2. This result pointed out that the incorporation of the as-prepared Au@TiO$_2$ NPs into porous TiO$_2$ and/or the perovskite capping layers had a negligible impact on the absorption enhancement. The results may be due to the extraordinarily high absorption coefficient of hybrid perovskite CH$_3$NH$_3$PbI$_3$ and the small amount of Au@TiO$_2$ core–shell NPs loaded on p-TiO$_2$ and/or perovskite capping layers. The increase in photocurrent density of plasmonic PSCs shown in Figure 3 and Table 1 was further explained by PL quenching. From Figure 4c, all absorber samples show emission peaks at about 761 nm (excitation wavelength 507 nm), corresponding to an absorption onset at ~760 nm.[39] The peak position of the emission was almost kept constant for all of the four absorber samples; however, their PL intensity and quenching changed a lot. The quenching effects indicated the facilitated charge transfer and separation induced by the LSPR. Compared to the case of the reference absorber without any modification, the PL intensity displayed a more and more intensely decreasing tendency from absorber 1 to absorber 3. Notably, the reference perovskite absorber sample exhibited the highest PL signal, and the corresponding PSC
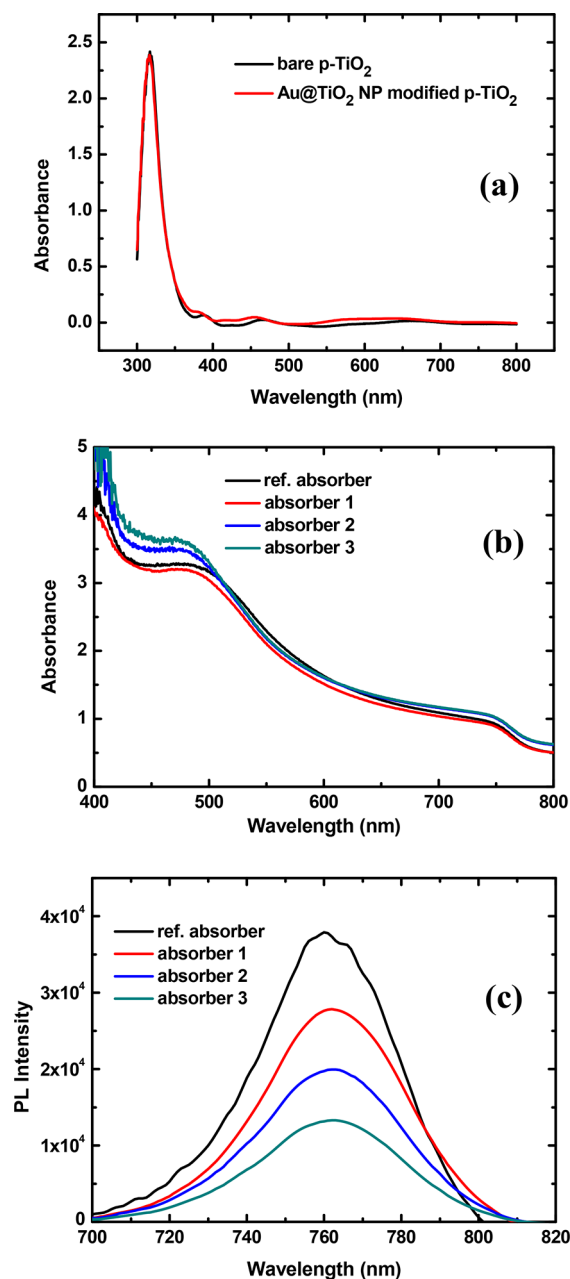

Figure 4. (a) UV/vis absorption of the porous TiO$_2$ films without and with Au@TiO$_2$ NP modification, (b) UV/vis absorption, and (c) PL spectra of p-TiO$_2$-based perovskite absorbers without and with Au@TiO$_2$ NP modification. Absorbers 1–3 with Au@TiO$_2$ NPs being blended within the p-TiO$_2$ layer, the perovskite capping layer, and both the p-TiO$_2$ and the capping perovskite films, respectively.

device was expected to show a higher recombination rate of carriers than the cells based on the other three absorber samples. An evidently stronger degree of PL quenching for both perovskite absorbers 1 and 2 with Au@TiO$_2$ NPs being blended within the p-TiO$_2$ layer, and the perovskite capping layer was observed, confirming that electron extraction efficiency from perovskite to TiO$_2$ electrode with Au@TiO$_2$ NP modification was more significant higher than the case based on the pristine TiO$_2$. This PL quenching also indicates that the rate of charge recombination is reduced drastically in Au@TiO$_2$ modified absorber. Absorber 3 with Au@TiO$_2$ NPs simultaneously incorporated into the p-TiO$_2$, and the perov-
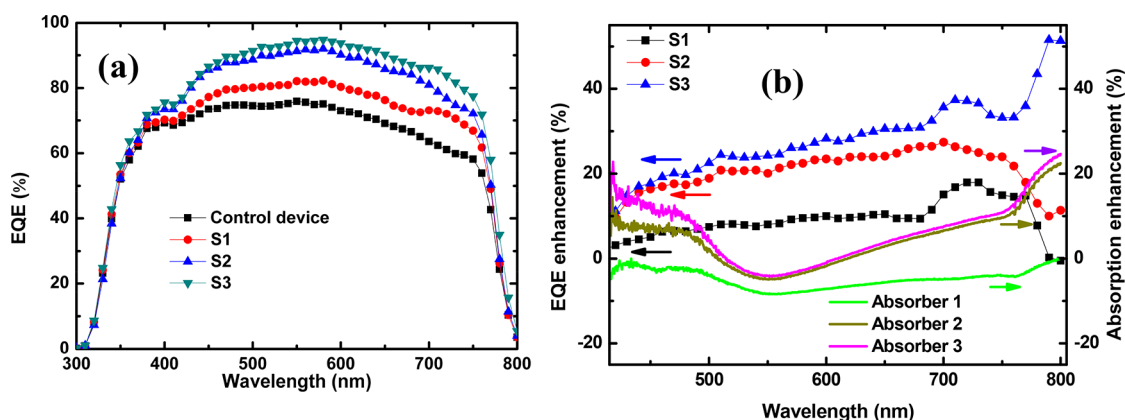
Figure 5. (a) EQE curves of the control (reference) device and plasmonic (S1−S3) PSCs. (b) EQE enhancements of plasmonic (S1−S3) PSCs and absorption variations of their absorbers: (left) EQE enhancement, $\Delta EQE/EQE_{ref}$ ($\Delta EQE = EQE_{plasmonic} − EQE_{ref}$, ΔEQE, the difference between EQE values of the reference and plasmonic devices); (right) absorption enhancement factors, $\Delta Abs/Abs_{ref}$ ($\Delta Abs = Abs_{plasmonic} − Abs_{ref}$, ΔAbs, the difference between absorption values of the reference and plasmonic absorber).

skite capping layers showed the lowest peak intensity and the most intense degree of PL quenching—a strong indication for the rapidest charge transfer, the most effective electron extraction, the least charge accumulation and the lowest recombination rate, and thus prospectively the highest short-circuit current and the best PV performance.[40,41] Therefore, the inclusion of Au@TiO$_2$ NPs into either the porous TiO$_2$ or the pure perovskite semiconductor is unambiguously helpful for improvements in the ability for charge separation and collection, rapid charge transport, low recombination rate, and enhanced photocurrent in the PSC device.

EQE is more pertinent than photocurrent−voltage measurement for studying optical and electrical responses of PSCs. EQE can be a product of light-harvesting efficiency, electron injection efficiency from excited perovskite CH$_3$NH$_3$PbI$_3$ to TiO$_2$ nanoparticles, and electron collection efficiency at the cathode in a mesoscopic CH$_3$NH$_3$PbI$_3$/TiO$_2$ heterojunction solar cell. Figure 5a shows the EQE spectra of four types of PSC devices (control device, S1−S3) as a function of the wavelength. Four devices show that the generation of photocurrent starts at ∼800 nm, which is in agreement with the band gap of MAPbI$_3$. Within the wavelength range from 400 to 750 nm, the photocurrent increased notably after incorporating the Au@TiO$_2$ NPs. The broad wavelength range of spectral response enhancement does not follow with the excitation range of Au NPs. Note that the absorption peak of the Au or Au@TiO$_2$ solution was located at approximately 550 nm (Figure 2). From Figure 5a, actually, three types of PSCs with Au@TiO$_2$ NP modification achieved higher EQE values than the control device without Au@TiO$_2$ NPs over the panchromatic wavelength range. Device S3 with Au@TiO$_2$ NPs simultaneously incorporated into the p-TiO$_2$, and the perovskite capping layer exhibits an absolute EQE of about 95%, whereas the control device based on bare TiO$_2$ and perovskite semiconductor displays an absolute EQE of ∼76% in the visible spectrum. The trends in the EQE follow those for the values of J_{SC} shown in Figure 3a and Table 1. The change in EQE enhancement for differently structured PSC devices is also consisted with those from J−V measurement and analysis.

Based on the EQE and absorption measurements shown in Figures 5a and 4b, compared to the case of the reference device without Au@TiO$_2$ modification, we further calculate the increase percentage in EQE ($\Delta EQE/EQE_{ref}$) and absorption ($\Delta Abs/Abs_{ref}$) with the addition of the Au@TiO$_2$ NPs, which we show in Figure 5b. From Figure 5b, although there are some features in the spectrum, the EQE enhancement is broadly distributed over the whole range and does not specifically follow the plasmon mode profile. The maximal absolute EQE value was obtained at 580 nm, which quite matches the absorption peak of Au@TiO$_2$ NPs and likely provides some evidence that the LSPR effects of Au nanostructures indeed induced improvements in the PCEs of PSCs. The maximal EQE enhancement (over 50%) was achieved at 790 nm for S3, which coincides with the absorption enhancement peak due to the scattering effect of 80 nm sized Au@TiO$_2$ NPs. Because 790 nm is the edge of the absorption band of perovskite film, the peak of $\Delta EQE/EQE_{ref}$ or $\Delta Abs/Abs_{ref}$ corresponding to the resonance of Au@TiO$_2$ NPs cannot be identified. In addition, the enhancement percentage obtained from the light absorption is tremendously lower than that of the EQE incremental quantity over the panchromatic wavelength range, as shown in Figure 5b. The broad enhancement in EQE suggests that the enhanced device performance of Au@TiO$_2$ composite PSCs mainly come from plasmonically enhanced electrical properties of the Au@TiO$_2$ photovoltaic composites (plasmonic electrical effects), rather than from optical effects alone. For three structured plasmonic PSCs with Au@TiO$_2$ modification, we unambiguously observed enhanced photocurrent from 400 to 750 nm, but no significant change to the light harvesting capability. Specially, in terms of device S1 with Au@TiO$_2$ NPs being blended within the p-TiO$_2$ layer, impressive EQE enhancement takes place over the visible regime (400−750 nm), and hence, its J_{SC} value considerably increases from 17.40 to 21.20 mA cm^{-2} shown Figure 3a and Table 1, whereas there is almost no light absorption enhancement. From Figure 3a and Table 1, P25 TiO$_2$ nanoparticles on their own do not enhance the photocurrent but rather reduce it. The results indicated that the plasmon-related light absorption contributed negligibly to either the EQE or J_{SC} enhancements. Thus, our conclusion is that Au@TiO$_2$ NPs enhance the solar cells internal conversion efficiency. The improvement could be mainly attributed to enhanced charge separation/free carrier generation, to augmented charge collection, and/or to the reduced charge recommendation rate.[20−25]
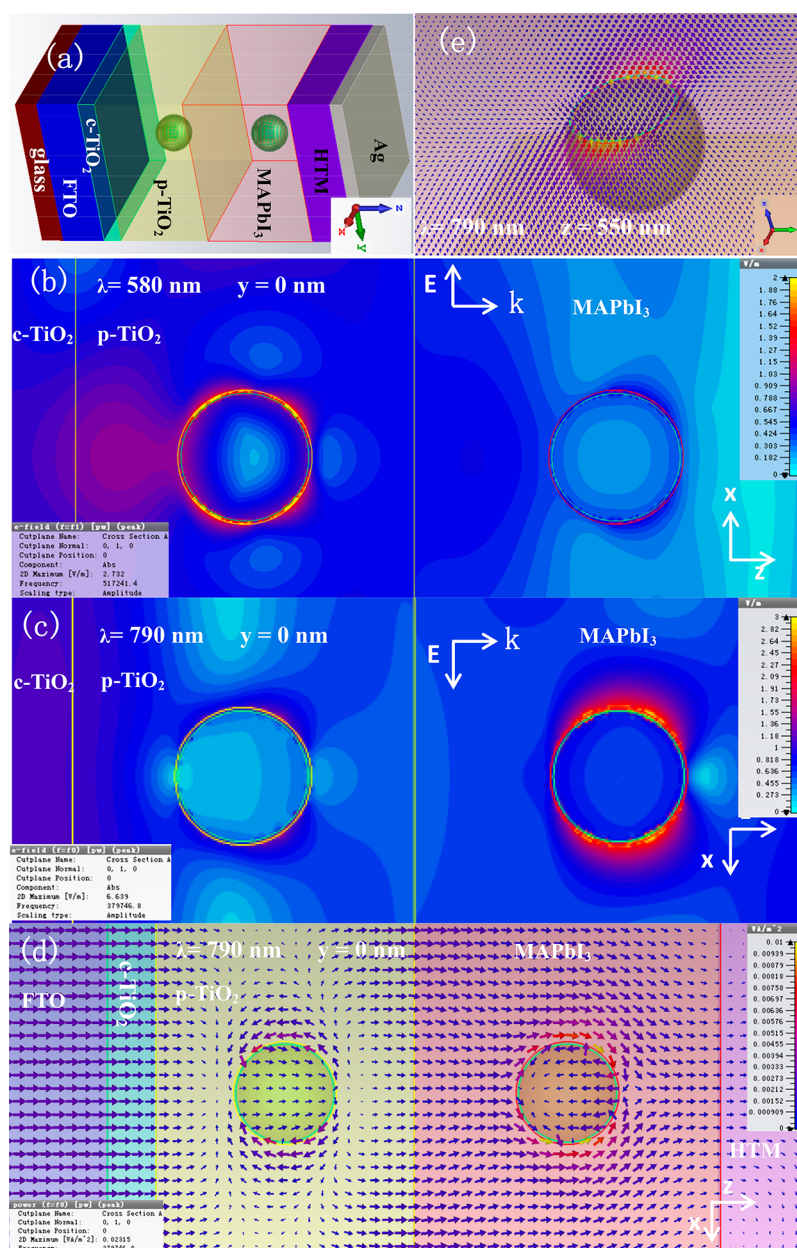
Figure 6. (a) Model of device modified with both Au@TiO$_2$ NPs. 2D field |E| enhancement distribution image in the xz-planes at (b) y = 0 nm, λ = 580 nm and (c) y = 0 nm, λ = 790 nm. 2D power flow diagrams within the xz-plane at (d) y = 0 nm, λ = 790 nm and the xy-plane at (e) z = 550 nm, λ = 790 nm.

To investigate the roles of Au@TiO$_2$ NPs in the observed EQE and photocurrent and PCE improvements in the plasmonic PSC cells, finite-difference time-domain (FDTD) numerical simulations were performed on a three-dimensional (3D) model. In the real PSC device, the absorber can be divided into porous and capping parts, the porous portion mainly consists of TiO$_2$, and the capping layer is pure MAPbI$_3$. Considering the real thicknesses of both p-TiO$_2$ and capping films, the sandwiched model consists of glass(50)/FTO(100)/c-TiO$_2$(40)/p-TiO$_2$(210)/MAPbI$_3$(250)/ HTM(100)/Ag(30), from the left to the right as shown in Figure 6a, and in which a single Au@TiO$_2$ sphere is embedded in the centers of p-TiO$_2$ and MAPbI$_3$ layers. The numbers in parentheses indicate the layer thicknesses in nanometers. The size of Au spheres (light green color) is 80 nm in diameter, and the thickness of TiO$_2$ shell is 2 nm. In order to see the Au@TiO$_2$ spheres, the colors

of both p-TiO$_2$(light green color) and capping MAPbI$_3$ (light blue color) are half transparent. The optical properties (refractive index, n, and extinction coefficient, k) of materials are from the data in previous publications.[42,43] A commercial FIT software package (CST Microwave Studio 2006) was used with Cartesian grids system (FDTD module).[16,44,45]

The boundary conditions along the x- and y-axis is set to be "periodic". Upon choosing periodic boundary setting and a suitably refined computational grid (the maximum grid length was chosen as wavelength/300 in the paper) in the simulation software, the corresponding numerical solution gives an accurate representation of the dynamics of the electromagnetic field. The origin of the coordinates is taken at the center of the front surface of the glass, and Au@TiO$_2$ spheres are placed along the z coordinate as shown in Figure 6a. The size of the modeling area in the xz-plane is 350 nm × 350 nm. Let the

plane-wave electromagnetic field of wave vector k be incident from the front surface of the glass substrate. The wave propagates along the z coordinate, the electric vector is along the x coordinate, and the magnetic vector is along the y coordinate. Figures 6b and 6c show the calculated local amplitude enhancement distribution of the electric field $|E|$ in the xz-plane at $y = 0$ for an incident wave with a wavelength of 580 or 790 nm, respectively. The maximal absolute EQE value was obtained at 580 nm, and the maximal EQE enhancement was at 790 nm for devices with Au@TiO$_2$ NP modification in Figures 5a,b. The circumferences of the Au@TiO$_2$ spheres within the p-TiO$_2$ and MAPbI$_3$ hosts can be distinctly observed from the calculated figures. Under visible light at 580 nm, the electric field $|E|$ is obviously enhanced and localized around the Au sphere embedded in the p-TiO$_2$ host, whereas the electric field is only slightly enhanced and confined around the Au sphere embedded in the capping MAPbI$_3$ host, as shown in Figure 6b. At longer wavelengths, the results are contrary. The electric field is less enhanced and confined around the Au sphere embedded in the p-TiO$_2$ host, while the electric field is significantly more enhanced and localized around the Au sphere embedded in the capping MAPbI$_3$ host, as shown in Figure 6c. The maximum $|E|$ enhancement factor is up to 2.7 and 7.8 at 580 and 790 nm, respectively. Devices S1 and S2 were made with Au@TiO$_2$ NPs blended within the p-TiO$_2$ and the perovskite capping hosts, respectively. The FDTD simulation results demonstrated that the LSPR effect led to a substantially nonuniform electric field distribution, which is greatly dependent on the wavelength of the incident light. However, this wavelength-dependent difference was not observed in the EQE or absorption testing measurements for the plasmonic devices S1 or S2, which further suggested that the J_{SC} enhancement cannot be attributed to the optical effect of the plasmonic nanoparticles but other effects.

Figures 6d and 6e show the simulated power flow onto the xz-plane at $y = 0$ and the xy-plane at $z = 550$ nm, deviated from the center ($z = 525$ nm) of the Au sphere embedded in the MAPbI$_3$, at a wavelength of 790 nm, respectively. When the near-infrared (NIR) light with a wavelength of 790 nm is normally incident on the PSC device from the front glass, the wave straight passes through c-TiO$_2$ layer and enters into the porous layer along the z coordinate. But, on the regions near and within the Au spheres, the straight propagation of light power flow is replaced by complex whirls and circulates round the Au spheres and the host material as shown in Figures 6d,e. The Au sphere absorbs lights via some portion of its surfaces and then reradiates energy into the absorber via other parts of the surfaces. Light power flows could circulate the near-field areas for multiple rounds due to interference of scattered and incident lights.[46] This energy flow regulation can open a process which is different from the widely reported light absorption enhancement by LSPRs[13−17,47] or hot-electron injection[28,48−50] for plasmon-enhanced solar energy harvesting. The plasmonic nanometal absorbs sunlight, converts the absorbed energy into LSPR oscillations, and transfers the plasmonic energy to the perovskite semiconductor, which generates electron−hole pairs below and near the perovskite semiconductor band edge[51,52] and enhances the efficiency of the incident photon-to-electron conversion process for NIR frequencies in perovskite solar cells shown in Table 1 and Figures 5a,b. On the other hand, when the LSPR phenomenon occurs, the accumulated energy on Au@TiO$_2$ nanospheres is also likely to dissipate in the form of re-emitted photons.

Because of the energy flow circulation and regulation shown in Figures 6d,e, photons are reabsorbed and re-emitted for many times before an electron−hole pair is collected or a luminescent red photon escapes. The radiated photons from exciton decay would have a dramatically prolonged optical path length due to the energy flow regulatory benefit of the Au nanospheres. By this means the reabsorption from reemitted light is enhanced, in essence enabling photon recycling with a much greater efficiency and driving the enhanced EQE and photocurrent in perovskite solar cells.[27,53−55] And the higher photon densities also lead to higher internal luminescence and a buildup of excited charges, which increase the split of quasi-Fermi levels and enhance the achievable open-circuit voltage in our plasmonic solar cells shown in Figure 3 and Table 1.

To further investigate the underlying mechanism responsible for the enhanced performance of the devices with Au@TiO$_2$ core−shell nanostructures, we examined and compared the maximum exciton generation rates (G_{max}) and exciton dissociation probabilities [$P(E,T)$] for devices prepared with or without Au@TiO$_2$ NP modification, following the analytical approach reported for plasmonic organic solar cells.[22,56] Figure 7 shows the effects of metal nanostructures on the photo-
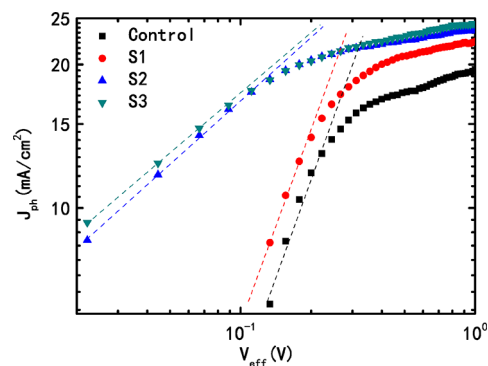

Figure 7. Plots of photocurrent density (J_{ph}) with respect to the effective bias (V_{eff}) in PSCs with different device structures.

current density (J_{ph}) of the cells. J_{ph} is defined as $J_{ph} = J_L − J_D$, where J_L and J_D are the current densities under illumination and in the dark, respectively. V_{eff} is determined as $V_{eff} = V_0 − V_a$, where V_0 is the voltage at which $J_{ph} = 0$ and V_a is the applied bias voltage. J_{ph} was found to increase linearly with V_{eff} in the low-V_{eff} range and to saturate gradually at high V_{eff}. From Figure 7, with increasing effective voltage, the photocurrent (J_{ph}) in the device S3 with Au@TiO$_2$ NPs being blended within both the p-TiO$_2$ layer and the perovskite capping layer saturated earlier than that in the control device. Generally, the saturated photocurrent (J_{sat}) is correlated with the maximum exciton generation rate (G_{max}), exciton dissociation probability, and carrier transport and charge collection probabilities in the high-V_{eff} range. G_{max} can be calculated from $J_{ph} = qG_{max}L$, where q is the electronic charge and L is the thickness of the active layer. The values of G_{max} for the control device and solar cells (S1, S2, S3) with Au nanostructures are 3.43×10^{27} m^{-3} s^{-1} ($J_{sat} = 195$ A/m^2), 3.94×10^{27} m^{-3} s^{-1} ($J_{sat} = 224$ A/m^2), 4.15×10^{27} m^{-3} s^{-1} ($J_{sat} = 236$ A/m^2), and 4.30×10^{27} m^{-3} s^{-1} ($J_{sat} = 244$ A/m^2), respectively. An obvious enhancement of G_{max} occurred after the incorporation of Au nanostructures. Considering the constant of absorbed incident photons for one cell, assuming that all of the photogenerated excitons are dissociated into free charge carriers in the high-V_{eff}

range, J_{sat} is then limited by the carrier transport and collection. The exciton dissociation probability $P(E,T)$ can be obtained from the normalized photocurrent density (J_{ph}/J_{sat}).[22,56] The $P(E,T)$ values of the devices (S1, S2, S3) with Au nanostructures increased to 96.4%, 97.2%, and 97.2% from 93.5% obtained for the control cells. PSC solar cells (S1−S3) with Au@TiO$_2$ NP modification show higher $P(E,T)$ values than the control device without Au@TiO$_2$ NP modification. The increase in the exciton generation rate and the exciton dissociation probability enhances free carrier generation/charge separation, reduces the recombination rate, enhances the carrier transport and collection, and therefore improves the J_{SC} and FF factors of plasmonic thin film solar cells. The results indicated that the presence of Au@TiO$_2$ nanospheres within the p-TiO$_2$ and/or the perovskite capping layers benefited generation of electron−hole pairs and the dissociation of excitons into free charge carriers, improving the carrier transport and collection probabilities. Actually, some previous studies about plasmonic PSCs also provided experimental evidence to support the results that the presence of metallic NPs favors photocarrier generation, separation, transfer, transport, or collection in PSCs.[28,30,47]

4. CONCLUSIONS

We have developed efficient plasmonic perovskite solar cells (PSCs) by embedding Au@TiO$_2$ core−shell nanoparticles (NPs) into porous TiO$_2$ and/or perovskite semiconductor capping layers. Optical, electrical, and electronic effects from metal nanostructures on the performance of PSCs were systematically investigated by a combined evaluation of surface morphologies of Au@TiO$_2$ modified perovskite capping and porous TiO$_2$ films, photovoltaic characteristics, photocurrent behavior, and steady-state photoluminescence (PL). The optimized structured device is obtained by simultaneously incorporating 80 nm sized Au@TiO$_2$ nanospheres into mesoporous titania and perovskite capping layers and delivers 18.24% efficiency, showing over 44% enhancement compared with the reference device without the metal NPs. The plasmonic enhancement mechanism is associated with improved exciton generation rate, enhanced exciton dissociation probability, and more efficient carrier transfer/collection induced by the LSPR effect. The results offer a possible method to dramatically enhance the performance of mesoporous PSC devices by employing metal nanostructures and provide further insight into the development of ideal plasmonic functionality for future optoelectronic systems.

AUTHOR INFORMATION

Corresponding Author
*E-mail: smhuang@phy.ecnu.edu.cn (S.H.).

ORCID
Xiaohong Chen: 0000-0003-0018-0198
Sumei Huang: 0000-0001-5283-3918

Notes
The authors declare no competing financial interest.

REFERENCES

(1) Kojima, A.; Teshima, K.; Shirai, Y.; Miyasaka, T. Organometal Halide Perovskites as Visible-Light Sensitizers for Photovoltaic Cells. *J. Am. Chem. Soc.* **2009**, *131*, 6050−6051.

(2) Lee, M. M.; Teuscher, J.; Miyasaka, T.; Murakami, T. N.; Snaith, H. J. Efficient Hybrid Solar Cells Based on Meso-Superstructured Organometal Halide Perovskites. *Science* **2012**, *338*, 643−647.

(3) Jeon, N. J.; Noh, J. H.; Yang, W. S.; Kim, Y. C.; Ryu, S.; Seo, J.; Seok, S. I. Compositional Engineering of Perovskite Materials for High-Performance Solar Cells. *Nature* **2015**, *517* (7535), 476−480.

(4) Green, M. A.; Emery, K.; Hishikawa, Y.; Warta, W.; Dunlop, E. D.; Levi, D. H.; Ho-Baillie, A. W. Y. Solar Cell Efficiency Tables (version 49). *Prog. Photovoltaics* **2017**, *25* (1), 3−13.

(5) Burschka, J.; Pellet, N.; Moon, S. J.; Humphry-Baker, R.; Gao, P.; Nazeeruddin, M. K.; Gratzel, M. Sequential Deposition as a Route to High-Performance Perovskite-Sensitized Solar Cells. *Nature* **2013**, *499* (7458), 316−319.

(6) Xiao, Z.; Bi, C.; Shao, Y.; Dong, Q.; Wang, Q.; Yuan, Y.; Wang, C.; Gao, Y.; Huang, J. Efficient, High Yield Perovskite Pphotovoltaic Devices Grown by Interdiffusion of Solution-Processed Precursor Stacking Layers. *Energy Environ. Sci.* **2014**, *7* (8), 2619−2623.

(7) Chen, Q.; Zhou, H.; Hong, Z.; Luo, S.; Duan, H. S.; Wang, H. H.; Liu, Y.; Li, G.; Yang, Y. Planar Heterojunction Perovskite Solar Cells via Vapor-Assisted Solution Process. *J. Am. Chem. Soc.* **2014**, *136* (2), 622−625.

(8) Liu, M.; Johnston, M. B.; Snaith, H. J. Efficient Planar Heterojunction Perovskite Solar Cells by Vapour Deposition. *Nature* **2013**, *501* (7467), 395−398.

(9) Jeon, N. J.; Noh, J. H.; Kim, Y. C.; Yang, W. S.; Ryu, S.; Seok, S. I. Solvent Engineering for High-Performance Inorganic-Organic Hybrid Perovskite Solar Cells. *Nat. Mater.* **2014**, *13* (9), 897−903.

(10) Zhang, C.; Luo, Y.; Chen, X.; Chen, Y.; Sun, Z.; Huang, S. Effective Improvement of the Photovoltaic Performance of Carbon-Based Perovskite Solar Cells by Additional Solvents. *Nano-Micro Lett.* **2016**, *8* (4), 347−357.

(11) Saliba, M.; Matsui, T.; Seo, J. Y.; Domanski, K.; Correa-Baena, J. P.; Nazeeruddin, M. K.; Zakeeruddin, S. M.; Tress, W.; Abate, A.; Hagfeldt, A.; Gratzel, M. Cesium-Containing Triple Cation Perovskite Solar cells: Improved Stability, Reproducibility and High Efficiency. *Energy Environ. Sci.* **2016**, *9* (6), 1989−1997.

(12) Li, J.; Cushing, S. K.; Meng, F.; Senty, T. R.; Bristow, A. D.; Wu, N. Plasmon-Induced Resonance Energy Transfer for Solar Energy Conversion. *Nat. Photonics* **2015**, *9* (9), 601−607.

(13) Ding, B.; Lee, B. J.; Yang, M.; Jung, H. S.; Lee, J.-K. Surface-Plasmon Assisted Energy Conversion in Dye-Sensitized Solar Cells. *Adv. Energy Mater.* **2011**, *1* (3), 415−421.

(14) Zhang, D.; Wang, M.; Brolo, A. G.; Shen, J.; Li, X.; Huang, S. Enhanced Performance of Dye-Sensitized Solar Cells Using Gold Nanoparticles Modified Fluorine Tin Oxide Electrodes. *J. Phys. D: Appl. Phys.* **2013**, *46* (2), 024005.

(15) Schaadt, D. M.; Feng, B.; Yu, E. T. Enhanced Semiconductor Optical Absorption via Surface Plasmon Excitation in Metal Nanoparticles. *Appl. Phys. Lett.* **2005**, *86* (6), 063106.

(16) Chen, Y. R.; Li, Z. Q.; Chen, X. H.; Liu, C.; Ye, X. J.; Wang, Z. B.; Sun, Z.; Huang, S. M. Improved Performance of Flexible Amorphous Silicon Solar Cells with Silver Nanowires. *J. Appl. Phys.* **2012**, *112* (12), 124320.

(17) Lee, J. H.; Park, J. H.; Kim, J. S.; Lee, D. Y.; Cho, K. High Efficiency Polymer Solar Cells with Wet Deposited Plasmonic Gold Nanodots. *Org. Electron.* **2009**, *10* (3), 416−420.

(18) Stenzel, O.; Stendal, A.; Voigtsberger, K.; von Borczyskowski, C. Enhancement of the Photovoltaic Conversion Efficiency of Copper Phthalocyanine Thin Film Devices by Incorporation of Metal Clusters. *Sol. Energy Mater. Sol. Cells* **1995**, *37*, 337−348.

(19) Morfa, A. J.; Rowlen, K. L.; Reilly, T. H.; Romero, M. J.; van de Lagemaat, J. Plasmon-Enhanced Solar Energy Conversion in Organic Bulk Heterojunction Photovoltaics. *Appl. Phys. Lett.* **2008**, *92* (1), 013504.

(20) Salvador, M.; MacLeod, B. A.; Hess, A.; Kulkarni, A. P.; Munechika, K.; Chen, J. I. L.; Ginger, D. S. Electron Accumulation on Metal Nanoparticles in Plasmon-Enhanced Organic Solar Cells. *ACS Nano* 2012, *6*, 10024−10032.

(21) Yang, X.; Chueh, C.-C.; Li, C.-Z.; Yip, H.-L.; Yin, P.; Chen, H.; Chen, W.-C.; Jen, A. K. Y. High-Efficiency Polymer Solar Cells Achieved by Doping Plasmonic Metallic Nanoparticles into Dual Charge Selecting Interfacial Layers to Enhance Light Trapping. *Adv. Energy Mater.* 2013, *3* (5), 666−673.

(22) Wang, J.; Jia, X.; Zhou, J.; Pan, L.; Huang, S.; Chen, X. Improved Performance of Polymer Solar Cells by Thermal Evaporation of AgAl Alloy Nanostructures into the Hole-Transport Layer. *ACS Appl. Mater. Interfaces* 2016, *8* (39), 26098−26104.

(23) Chan, K.; Wright, M.; Elumalai, N.; Uddin, A.; Pillai, S. Plasmonics in Organic and Perovskite Solar Cells: Optical and Electrical Effects. *Adv. Opt. Mater.* 2017, *5*, 1600698.

(24) Liu, C. M.; Chen, C. M.; Su, Y. W.; Wang, S. M.; Wei, K. H. The Dual Localized Surface Plasmonic Effects of Gold Nanodots and Gold Nanoparticles Enhance the Performance of Bulk Heterojunction Polymer Solar Cells. *Org. Electron.* 2013, *14*, 2476−2483.

(25) Lee, K. C. J.; Chen, Y.; Lin, H.; Cheng, C.; Chen, P.; Wu, T.; Shih, M.; Wei, K.; Li, L.; Chang, C. Plasmonic Gold Nanorods Coverage Influence on Enhancement of the Photoluminescence of Two-Dimensional MoS₂ Monolayer. *Sci. Rep.* 2015, *5*, 16374.

(26) Zhang, W.; Saliba, M.; Stranks, S. D.; Sun, Y.; Shi, X.; Wiesner, U.; Snaith, H. J. Enhancement of Perovskite-Based Solar Cells Employing Core-Shell Metal Nanoparticles. *Nano Lett.* 2013, *13* (9), 4505−4510.

(27) Saliba, M.; Zhang, W.; Burlakov, V. M.; Stranks, S. D.; Sun, Y.; Ball, J. M.; Johnston, M. B.; Goriely, A.; Wiesner, U.; Snaith, H. J. Plasmonic-Induced Photon Recycling in Metal Halide Perovskite Solar Cells. *Adv. Funct. Mater.* 2015, *25* (31), 5038−5046.

(28) Yuan, Z.; Wu, Z.; Bai, S.; Xia, Z.; Xu, W.; Song, T.; Wu, H.; Xu, L.; Si, J.; Jin, Y.; Sun, B. Hot-Electron Injection in a Sandwiched TiOₓ-Au-TiOₓ Structure for High-Performance Planar Perovskite Solar Cells. *Adv. Energy Mater.* 2015, *5* (10), 1500038.

(29) Cheng, Y.; Chen, C.; Chen, X.; Jin, J. J.; Li, H.; Song, H. W.; Dai, Q. L. Considerably Enhanced Perovskite Solar Cells via the Introduction of Metallic Nanostructures. *J. Mater. Chem. A* 2017, *5* (14), 6515−6521.

(30) Lee, D. S.; Kim, W.; Cha, B. G.; Kwon, J.; Kim, S. J.; Kim, M.; Kim, J.; Wang, D. H.; Park, J. H. Self-Position of Au NPs in Perovskite Solar Cells: Optical and Electrical Contribution. *ACS Appl. Mater. Interfaces* 2016, *8* (1), 449−454.

(31) Zhang, C.; Luo, Q.; Shi, J.; Yue, L.; Wang, Z.; Chen, X.; Huang, S. Efficient Perovskite Solar Cells by Combination Use of Au Nanoparticles and Insulating Metal Oxide. *Nanoscale* 2017, *9* (8), 2852−2864.

(32) Kuznetsov, A. I.; Miroshnichenko, A. E.; Brongersma, M. L.; Kivshar, Y. S.; Luk'yanchuk, B. Optically Resonant Dielectric Nanostructures. *Science* 2016, *354* (6314), aag2472.

(33) Zhang, P.; Wu, P.; Bao, S.; Wang, Z.; Tian, B.; Zhang, J. Synthesis of Sandwich-Structured AgBr@Ag@TiO₂ Composite Photocatalyst and Study of its Photocatalytic Performance for the Oxidation of Benzyl Alcohols to Benzaldehydes. *Chem. Eng. J.* 2016, *306*, 1151−1161.

(34) Fang, C.-H.; Jia, H.-L.; Chang, S.; Ruan, Q.-F.; Wang, P.; Chen, T.; Wang, J.-F. (Gold Core)/(Titania Shell) Nanostructures for Plasmon-Enhanced Photon Harvesting and Generation of Reactive Oxygen Species. *Energy Environ. Sci.* 2014, *7*, 3431−3438.

(35) Jiang, Z.; Chen, X.; Lin, X.; Jia, X.; Wang, J.; Pan, L.; Huang, S.; Zhu, F.; Sun, Z. Amazing Stable Open-Circuit Voltage in Perovskite Solar Cells Using AgAl Alloy Electrode. *Sol. Energy Mater. Sol. Cells* 2016, *146*, 35−43.

(36) Zhu, Z.; Chang, J.; Wu, R. Fast Ozone Detection by Using a Core-Shell Au@TiO₂ Sensor at Room Temperature *Sens. Sens. Actuators, B* 2015, *214*, 56−62.

(37) Wang, D. H.; Kim, D. Y.; Choi, K. W.; Seo, J. H.; Im, S. H.; Park, J. H.; Park, O. O.; Heeger, A. J. Enhancement of Donor-Acceptor

(38) Catchpole, K. R.; Polman, A. Plasmonic Solar Cells. *Opt. Express* 2008, *16*, 21793−21800.

(39) Im, J. H.; Lee, C. R.; Lee, J. W.; Park, S. W.; Park, N. G. 6.5% Efficient Perovskite Quantum-Dot-Sensitized Solar Cell. *Nanoscale* 2011, *3* (10), 4088−4093.

(40) Zhu, G.; Lin, T.; Lü, X.; Zhao, W.; Yang, C.; Wang, Z.; Yin, H.; Liu, Z.; Huang, F.; Lin, J. Black Brookite Titania with High Solar Absorption and Excellent Photocatalytic Performance. *J. Mater. Chem. A* 2013, *1* (34), 9650−9653.

(41) Huang, C.; Liu, C.; Di, Y.; Li, W.; Liu, F.; Jiang, L.; Li, J.; Hao, X.; Huang, H. Efficient Planar Perovskite Solar Cells with Reduced Hysteresis and Enhanced Open Circuit Voltage by Using PW12-TiO₂ as Electron Transport Layer. *ACS Appl. Mater. Interfaces* 2016, *8* (13), 8520−8526.

(42) Ball, J. M.; Stranks, S. D.; Hörantner, M. T.; Hüttner, S.; Zhang, W.; Crossland, E. J. W.; Ramirez, I.; Riede, M.; Johnston, M. B.; Friend, R. H.; Snaith, H. J. Optical Properties and Limiting Photocurrent of Thin-Film Perovskite Solar Cells. *Energy Environ. Sci.* 2015, *8* (2), 602−609.

(43) Palik, E. D.; Ghosh, G. *Electronic Handbook of Optical Constants of Solids*; SciVision, Academic: New York, 1999.

(44) Fan, W.; Yan, B.; Wang, Z.; Wu, L. Three-Dimensional All-Dielectric Metamaterial Solid Immersion Lens for Subwavelength Imaging at Visible Frequencies. *Sci. Adv.* 2016, *2*, e1600901.

(45) Luo, Q.; Chen, Y.; Li, Z.; Zhu, F.; Chen, X.; Sun, Z.; Wei, Y.; Guo, H.; Wang, Z. B.; Huang, S. Large Enhancements of NaYF₄:Yb/Er/Gd Nanorod Upconversion Emissions via Coupling with Localized Surface Plasmon of Au Film. *Nanotechnology* 2014, *25* (18), 185401.

(46) Bashevoy, M. V.; Fedotov, V. A.; Zheludev, N. I. Optical Whirlpool on an Absorbing Metallic Nanoparticle. *Opt. Express* 2005, *13*, 8372−8379.

(47) Mali, S. S.; Shim, C. S.; Kim, H.; Patil, P. S.; Hong, C. K. In Situ Processed Gold Nanoparticle-Embedded TiO₂ Nanofibers Enabling Plasmonic Perovskite Solar Cells to Exceed 14% Conversion Efficiency. *Nanoscale* 2016, *8* (5), 2664−2677.

(48) Furube, A.; Du, L.; Hara, K.; Katoh, R.; Tachiya, M. Ultrafast Plasmon-Induced Electron Transfer from Gold Nanodots into TiO₂ Nanoparticles. *J. Am. Chem. Soc.* 2007, *129*, 14852−14853.

(49) Giugni, A.; Torre, B.; Toma, A.; Francardi, M.; Malerba, M.; Alabastri, A.; Proietti Zaccaria, R.; Stockman, M. I.; Di Fabrizio, E. Hot-Electron Nanoscopy Using Adiabatic Compression of Surface Plasmons. *Nat. Nanotechnol.* 2013, *8* (11), 845−852.

(50) Zhu, Z.; Ma, J.; Wang, Z.; Mu, C.; Fan, Z.; Du, L.; Bai, Y.; Fan, L.; Yan, H.; Phillips, D. L.; Yang, S. Efficiency Enhancement of Perovskite Solar Cells Through Fast Electron Extraction: the Role of Graphene Quantum Dots. *J. Am. Chem. Soc.* 2014, *136* (10), 3760−3763.

(51) Cushing, S. K.; Li, J.; Meng, F.; Senty, T. R.; Suri, S.; Zhi, M.; Li, M.; Bristow, A. D.; Wu, N. Photocatalytic Activity Enhanced by Plasmonic Resonant Energy Transfer from Metal to Semiconductor. *J. Am. Chem. Soc.* 2012, *134* (36), 15033−15041.

(52) Li, J.; Cushing, S. K.; Zheng, P.; Meng, F.; Chu, D.; Wu, N. Plasmon-Induced Photonic and Energy-Transfer Enhancement of Solar Water Splitting by a Hematite Nanorod Array. *Nat. Commun.* 2013, *4*, 2651.

(53) Pazos-Outón, L. M.; Szumilo, M.; Lamboll, R.; Richter, J. M.; Crespo-Quesada, M.; Abdi-Jalebi, M.; Beeson, H. J.; Vrucinic, M.; Alsari, M.; Snaith, H. J.; Ehrler, B.; Friend, R. H.; Deschler, F. Photon Recycling in Lead Iodide Perovskite Solar Cells. *Science* 2016, *351* (6280), 1430−1433.

(54) Even, J.; Pedesseau, L.; Katan, C. Analysis of Multivalley and Multibandgap Absorption and Enhancement of Free Carriers Related to Exciton Screening in Hybrid Perovskites. *J. Phys. Chem. C* 2014, *118* (22), 11566−11572.

(55) Lin, Q.; Armin, A.; Nagiri, R. C. R.; Burn, P. L.; Meredith, P. Electro-Optics of Perovskite Solar Cells. *Nat. Photonics* **2014**, *9*, 106−112.

(56) Shrotriya, V.; Yao, Y.; Li, G.; Yang, Y. Effect of Self-Organization in Polymer/Fullerene Bulk Heterojunctions on Solar Cell Performance. *Appl. Phys. Lett.* **2006**, *89* (6), 063505.